IEEE Access
Multidisciplinary ⋮ Rapid Review ⋮ Open Access Journal

Received June 19, 2020, accepted June 27, 2020, date of publication July 1, 2020, date of current version July 15, 2020.

Digital Object Identifier 10.1109/ACCESS.2020.3006341

Single- and Multi-Frequency Direct Sampling Methods in a Limited-Aperture Inverse Scattering Problem

SANGWOO KANG[1], MARC LAMBERT[2,3], CHI YOUNG AHN[4], TAEYOUNG HA[4], AND WON-KWANG PARK[5]

[1]Chaire C2M, LTCI, Télécom Paris, 91120 Palaiseau, France
[2]Université Paris-Saclay, CentraleSupélec, CNRS, Laboratoire de Génie Electrique et Electronique de Paris, 91192 Gif-sur-Yvette, France
[3]Sorbonne Université, CNRS, Laboratoire de Génie Electrique et Electronique de Paris, 75252 Paris, France
[4]National Institute for Mathematical Sciences, Daejeon 34047, South Korea
[5]Department of Information Security, Cryptology, and Mathematics, Kookmin University, Seoul 02707, South Korea

Corresponding author: Won-Kwang Park (parkwk@kookmin.ac.kr)

This work was supported in part by the National Institute for Mathematical Sciences (NIMS) funded by the Korean Government under Grant NIMS-B20900000, and in part by the National Research Foundation of Korea (NRF) funded by the Ministry of Science and ICT (MSIT), Korea Government under Grant NRF-2020R1A2C1A01005221.

ABSTRACT Although the direct sampling method (DSM) has demonstrated its feasibility and robustness for imaging of small inhomogeneities, mathematical analyses of DSM have been conducted only on the full-aperture inverse scattering problem. Numerous studies have shown that DSM can also be applied in the limited-aperture inverse scattering problem, but most of its applications are still heuristic. This study considers an application, mathematical analysis, and improvement of DSM with a single-incident field only in the limited-aperture inverse scattering problem. First, we introduce a traditional indicator function of DSM at a single frequency, establish its mathematical structure, and examine its inherent limitation. To demonstrate the theoretical result, various results of numerical simulations with synthetic and experimental data are presented. Next, we consider the multi-frequency indicator function of DSM with a single-incident direction to improve imaging performance. For this, we design a multi-frequency indicator function of MDSM, analyze its mathematical structure, and theoretically explain the improvement of the imaging of single inhomogeneity and the limitation on the identification of multiple inhomogeneities. Various numerical simulations with synthetic and experimental data are presented to validate our results.

INDEX TERMS Direct sampling method, limited-aperture inverse scattering problem, numerical simulations, structure of indicator function.

I. INTRODUCTION

The main goal of the inverse scattering problem is to determine the unknown targets, such as location, shape, and/or other physical properties, from the collected scattered fields or far-field patterns. Owing to its various potential applications, for example, defects identifications in bridges and concrete walls [1]–[3], non-destructive testing [4]–[6], and biomedical imaging such as breast cancer detection [7]–[9] and brain imaging [10]–[12], numerous scientists, engineers, and so on have been studying this problem recently. In various real-world applications such as ground-penetrating radar [13]–[15], synthetic aperture radar [16]–[18], and seismic imaging [19]–[21], the range of incident and observation directions must be restricted. This is known as a limited-aperture inverse scattering problem. Unfortunately, this interesting problem is very difficult to solve because of its inherent nonlinearity and ill-posedness. Consequently, various algorithms have been developed to solve this problem, including iterative methods for minimizing the norm between the measurement data and the one provided by a numerical model miming the presence of true and man-made targets [7], [22]–[24]. However, in such iterative methods, a good initial guess is required to avoid either a very large number of iterations or being trapped in a local minimum.

To overcome these limitations and obtain a good initial guess, various non-iterative methods have been investigated that involve various limited-aperture inverse

The associate editor coordinating the review of this manuscript and approving it for publication was Yi Zhang.

scattering problems, for example, MUltiple SIgnal Classification (MUSIC) [25]–[27], Kirchhoff and subspace migrations [28]–[30], and topological derivatives [31]–[33]. One can refer to [34]–[40] for various inversion techniques applied in limited-aperture inverse scattering problems. It is noteworthy that these techniques yield very good results with a large number of incident waves and their corresponding scattered fields, whereas their performances decrease when the number of the incident waves is not sufficiently large [41]–[44]. Furthermore, we need additional operations, such as singular value decomposition, and careful threshold of nonzero singular values (subspace migration), as well as generation of projection operator onto the noise subspace through a careful threshold of nonzero singular values (MUSIC), or solving an adjoint problem (topological derivative).

Direct sampling method (DSM) is also a non-iterative technique utilized for identifying the location of small targets or outlining the shape of extended targets. In contrast to the other methods, DSM requires either one or a few incident fields for imaging and is very fast because it does not need any additional operations. Additionally, it turned out that DSM is a stable and robust technique in an inverse scattering problem. One can refer to [45]–[51] for a detailed description, application, advantages, and fundamental limitations. Recently, some authors investigated the mathematical structure of the DSM indicator function, proposed an improved version, and verified its relationship with the Kirchhoff migration in full-aperture inverse scattering problem [52]. Meanwhile, it has been applied heuristically in the limited-aperture inverse scattering problem; hence, there is a need to perform a rigorous analysis to establish the mathematical structure of DSM. This is the motivation of this study.

In this paper, we consider a DSM with a single-incident direction to identify two-dimensional small or large dielectric inhomogeneities in the limited-aperture inverse scattering problem. We first investigate the mathematical structure of an indicator function of DSM by establishing a relationship with a Bessel function of integer order of the first kind, the range of observation directions, and physical property about inhomogeneities (location, shape, size, etc). We also explain the unexplored intrinsic properties of DSM. Simulation results using synthetic data corrupted by random noise and real data [53] are exhibited to support theoretical results and demonstrate the effectiveness and limitations. Moreover, we introduce a multi-frequency indicator function of DSM (MDSM) for an improvement in the DSM. In contrast to numerous previously conducted studies, MDSM is effective for imaging small single inhomogeneity, but it is not effective for many small inhomogeneities. To explain the theory behind this, we investigate a mathematical theory of a multi-frequency indicator function by establishing a relationship with Bessel functions, Struve functions, Legendre polynomials, generalized hypergeometric functions, the range of incident and observation directions, and physical property of targets. As in the single-frequency case, the considered multi-frequency indicator functions are compared using numerical simulations with synthetic and experimental data.

Let us emphasize that orthogonality sampling method is also an effective and stable non-iterative technique, which requires either one or a few incident fields [54]–[57], and is very similar to the DSM [58]. This issue, though important it may be, seems to be outside the scope of this research.

This paper is organized as follows. In section II, we briefly introduce the basic concept of the direct-scattering problem and asymptotic expansion formula for the far-field pattern in the presence of small inhomogeneities. The structure analysis of the DSM indicator function at a single frequency and its corresponding numerical simulation results are presented in sections III and IV, respectively. The indicator function of DSM using multiple frequencies is designed and analyzed, and corresponding numerical simulation results are shown in section V. Section VI presents the conclusions and perspectives.

II. A TWO-DIMENSIONAL DIRECT-SCATTERING PROBLEM AND ASYMPTOTIC FORMULA

In this section, we briefly survey the two-dimensional direct-scattering problem from small dielectric inhomogeneities Σ_m denoted by $\Sigma_m = \mathbf{r}_m + \alpha_m \mathbf{D}_m$, for $m = 1, 2, \cdots, M$, where $\mathbf{r}_m$ denotes the location of the m^{th} dielectric inhomogeneities, α_m denotes its size, and $\mathbf{D}_m$ characterizes the shape of Σ_m. Let Σ denote the collection of all inhomogeneities, i.e., $\Sigma = \bigcup_m \Sigma_m$. Throughout this paper, we assume that all inhomogeneities are well-separated from each other. Let $\omega = 2\pi f$ denote the angular frequency, and ε_m and μ_m denote the dielectric permittivity and magnetic permeability of Σ_m, respectively, while ε_{b} and μ_{b} denote those of the background. Herein, we assume that all inhomogeneities are non-magnetic (i.e., the value of magnetic permeability is constant such that $\mu_m \equiv \mu_{\text{b}} = 1.256 \times 10^{-6}$ H/m). The piecewise constant permittivity $\varepsilon(\mathbf{x})$ can be defined as follows:

$$\varepsilon(\mathbf{x}) = \begin{cases} \varepsilon_m & \text{for } \mathbf{x} \in \Sigma_m \\ \varepsilon_{\text{b}} & \text{for } \mathbf{x} \in \mathbb{R}^2 \backslash \overline{\Sigma} \end{cases}$$

Using this, we define the free-space wavenumber, $k = \omega\sqrt{\varepsilon_{\text{b}}\mu_{\text{b}}}$.

Herein, we consider the plane-wave illumination, i.e., we set the incident field as $u_{\text{inc}}(\mathbf{x}, \mathbf{d}) = e^{ik\mathbf{d}\cdot\mathbf{x}}$, where $\mathbf{d} \in \mathbb{S}^1$ denotes the propagation direction, and $\mathbb{S}^1$ denotes the two-dimensional unit circle centered at the origin. Let $u(\mathbf{x}, \mathbf{d})$ denote the time-harmonic total field with transmission condition on the boundary of Σ_m that satisfies the following Helmholtz equation:

$$\Delta u(\mathbf{x}, \mathbf{d}) + \omega^2 \varepsilon(\mathbf{x}) \mu_{\text{b}} u(\mathbf{x}, \mathbf{d}) = 0.$$

The total field can be expressed as a sum of the incident and scattered field, $u(\mathbf{x}, \mathbf{d}) = u_{\text{inc}}(\mathbf{x}, \mathbf{d}) + u_{\text{scat}}(\mathbf{x}, \mathbf{d})$. To guarantee the uniqueness of solution, the scattered field must satisfy the

following Sommerfeld radiation condition:

$$\lim_{|\mathbf{x}|\to\infty}\sqrt{|\mathbf{x}|}\left(\frac{\partial u_{\text{scat}}(\mathbf{x},\mathbf{d})}{\partial|\mathbf{x}|}-iku_{\text{scat}}(\mathbf{x},\mathbf{d})\right)=0$$

uniformly in all directions $\hat{\mathbf{x}}=\mathbf{x}/|\mathbf{x}|\in\mathbb{S}^1$.

The scattered field, $u_{\text{scat}}(\mathbf{x},\mathbf{d})$, can be represented by a single-layer potential with unknown density $\phi_m(\mathbf{r},\mathbf{d})$ related to Σ (see [59] for the details) as follows:

$$u_{\text{scat}}(\mathbf{x},\mathbf{d})=-\frac{i}{4}\int_{\Sigma}H_0^{(1)}(k\,|\mathbf{x}-\mathbf{r}|)\varphi(\mathbf{r},\mathbf{d})d\mathbf{r},$$

where $H_0^{(1)}$ denotes the Hankel function of order zero of the first kind. We denote $u_\infty(\boldsymbol{\theta},\mathbf{d})$ be the far-field pattern of scattered field that is defined on $\mathbb{S}^1$. Then, following [60], $u_\infty(\boldsymbol{\theta},\mathbf{d})$ satisfies the following equation:

$$u_{\text{scat}}(\mathbf{x},\mathbf{d})=\frac{e^{ik|\mathbf{x}|}}{\sqrt{|\mathbf{x}|}}\left\{u_\infty(\boldsymbol{\theta},\mathbf{d})+O\left(\frac{1}{\sqrt{|\mathbf{x}|}}\right)\right\}\tag{1}$$

uniformly in all directions, $\boldsymbol{\theta}=\mathbf{x}/|\mathbf{x}|\in\mathbb{S}^1$. Based on [59], [60] and asymptotic form of Hankel function, $u_\infty(\boldsymbol{\theta},\mathbf{d})$ can be expressed as a single-layer potential with unknown density function, $\varphi(\mathbf{r},\mathbf{d})$:

$$u_\infty(\boldsymbol{\theta},\mathbf{d})=\frac{1+i}{4\sqrt{k\pi}}\int_{\Sigma}e^{-ik\boldsymbol{\theta}\cdot\mathbf{r}}\varphi(\mathbf{r},\mathbf{d})d\mathbf{r}.\tag{2}$$

Since the exact form of density function $\varphi(\mathbf{r},\mathbf{d})$ of equation (2) is unknown, we cannot design an indicator function of DSM at this stage. Now, let us assume that the following relationship holds, for all $m=1,2,\cdots,M$:

$$\alpha_m\sqrt{\frac{\varepsilon_m}{\varepsilon_{\text{b}}}}\ll\frac{\lambda}{2},\tag{3}$$

where λ denotes the given wavelength. Therefore, based on [61], Σ_m can be regarded as a small inhomogeneity, so the far-field pattern can be represented by the following asymptotic expansion formula below. In the sequel, this will play a key role in designing the indicator function of DSM.

Lemma 1 (Asymptotic Expansion Formula [60]): Assume that condition (3) *holds. Then,* $u_\infty(\boldsymbol{\theta},\mathbf{d})$ *can be represented by the following asymptotic expansion formula:*

$$u_\infty(\boldsymbol{\theta},\mathbf{d})\approx\frac{k^2(1+i)}{4\sqrt{k\pi}}\sum_{m=1}^{M}\mathcal{E}_m e^{ik\mathbf{r}_m\cdot(\mathbf{d}-\boldsymbol{\theta})},\tag{4}$$

where

$$\mathcal{E}_m=\alpha_m^2\,\text{area}(\mathbf{D}_m)\left(\frac{\varepsilon_m-\varepsilon_{\text{b}}}{\sqrt{\varepsilon_{\text{b}}\mu_{\text{b}}}}\right).$$

Here $\text{area}(\mathbf{D}_m)$ *denotes the area of* $\mathbf{D}_m$.

III. SINGLE-FREQUENCY DSM IN A LIMITED-APERTURE PROBLEM

In the limited-aperture problem, we define the following finite set of observation directions, $\mathbb{S}^1_{\text{obs}}$:

$$\mathbb{S}^1_{\text{obs}}=\{\boldsymbol{\theta}_n=(\cos\theta_n,\sin\theta_n):n=1,2,\cdots,N\}\subset\mathbb{S}^1,$$

where

$$\theta_n=\theta_1+(\theta_N-\theta_1)\frac{n-1}{N-1}.$$

Then, based on the traditional DSM [45], [46], [52], the indicator function of DSM in a limited-aperture configuration can be introduced as follows: for $\mathbf{z}\in\Omega$ and a fixed incident direction $\mathbf{d}$,

$$\mathfrak{F}_{\text{DSM}}(\mathbf{z})=\frac{|\langle u_\infty(\boldsymbol{\theta}_n,\mathbf{d}),e^{-ik\boldsymbol{\theta}_n\cdot\mathbf{z}}\rangle_{L^2(\mathbb{S}^1_{\text{obs}})}|}{||u_\infty(\boldsymbol{\theta}_n,\mathbf{d})||_{L(\mathbb{S}^1_{\text{obs}})}||e^{-ik\boldsymbol{\theta}_n\cdot\mathbf{z}}||_{L^2(\mathbb{S}^1_{\text{obs}})}},\tag{5}$$

where Ω denotes the region of interest (ROI). Here, the inner product and its corresponding norm are given by

$$\langle f(\boldsymbol{\theta}_n),g(\boldsymbol{\theta}_n)\rangle_{L^2(\mathbb{S}^1_{\text{obs}})}=\sum_{n=1}^{N}f(\boldsymbol{\theta}_n)\overline{g(\boldsymbol{\theta}_n)}$$

and

$$\|f(\boldsymbol{\theta})\|^2_{L^2(\mathbb{S}^1_{\text{obs}})}=\langle f(\boldsymbol{\theta}),f(\boldsymbol{\theta})\rangle_{L^2(\mathbb{S}^1_{\text{obs}})},$$

respectively.

Based on definition (5) and several previously conducted studies [45], [46], [52], the location of all inhomogeneities, Σ_m, must be identified via the map of $\mathfrak{F}_{\text{DSM}}(\mathbf{z})$ because $\mathfrak{F}_{\text{DSM}}(\mathbf{z})=1$ at $\mathbf{z}=\mathbf{r}_m\in\Sigma_m$ and $0\le\mathfrak{F}_{\text{DSM}}(\mathbf{z})<1$ at $\Omega\backslash\overline{\Sigma}$. However, in the limited-aperture problem, its results are quite different from those of the traditional studies; thus, a new analysis of the indicator function of DSM is needed. In the sequel, we derive the mathematical structure of indicator function, $\mathfrak{F}_{\text{DSM}}(\mathbf{z})$. Before starting this derivation, we recall a useful result derived in [29, Theorem 4.1] that demonstrates a relationship between an exponential function and an infinite series of Bessel functions of integer order.

Lemma 2: Let $\mathbf{z}=|\mathbf{z}|(\cos\phi,\sin\phi)\in\mathbb{R}^2$ *and* $\boldsymbol{\theta}=(\cos\theta,\sin\theta)\in\mathbb{S}^1_{\text{obs}}$. *Then, for sufficiently large* N, *the following relationship holds uniformly:*

$$\begin{aligned}\sum_{n=1}^{N}e^{ik\boldsymbol{\theta}_n\cdot\mathbf{z}}&\approx\int_{\mathbb{S}^1_{\text{obs}}}e^{ik\boldsymbol{\theta}\cdot\mathbf{z}}d\boldsymbol{\theta}=(\theta_N-\theta_1)J_0(k|\mathbf{z}|)\\&\quad+4\sum_{s=1}^{\infty}\frac{i^s}{s}J_s(k|\mathbf{z}|)\cos\frac{s\,(\theta_N+\theta_1-2\phi)}{2}\\&\quad\times\sin\frac{s(\theta_N-\theta_1)}{2}.\end{aligned}\tag{6}$$

Using the asymptotic formula (4) and equation (6), the mathematical structure of the DSM indicator function (theorem 1) can be obtained.

Theorem 1: Assume that the total number of observation directions, N, *is sufficiently large. Let* $\mathbf{r}_m-\mathbf{z}=|\mathbf{r}_m-\mathbf{z}|(\cos\phi_m,\sin\phi_m)$. *Then, the DSM indicator function can be represented as follows:*

$$\mathfrak{F}_{\text{DSM}}(\mathbf{z})\approx\frac{|\Phi_1(\mathbf{z},k)+\Lambda_1(\mathbf{z},k)|}{\max\limits_{\mathbf{z}\in\Omega}|\Phi_1(\mathbf{z},k)+\Lambda_1(\mathbf{z},k)|},\tag{7}$$

where

$$\Phi_1(\mathbf{z},k)=\sum_{m=1}^{M}\mathcal{E}_m e^{ik\mathbf{d}\cdot\mathbf{r}_m}J_0(k|\mathbf{r}_m-\mathbf{z}|) \tag{8}$$

and

$$\Lambda_1(\mathbf{z},k)=\frac{4}{\theta_N-\theta_1}\sum_{m=1}^{M}\mathcal{E}_m e^{ik\mathbf{d}\cdot\mathbf{r}_m}\sum_{s=1}^{\infty}\frac{i^s}{s}J_s(k|\mathbf{r}_m-\mathbf{z}|)\times\cos\frac{s\,(\theta_N+\theta_1-2\phi_m)}{2}\sin\frac{s(\theta_N-\theta_1)}{2}. \tag{9}$$

Proof: By applying the asymptotic formula of far-field pattern (4) to indicator function (5), we evaluate

$$\begin{aligned}&\langle u_\infty(\boldsymbol{\theta},\mathbf{d}),e^{-ik\boldsymbol{\theta}\cdot\mathbf{z}}\rangle_{L^2(\mathbb{S}^1_{\text{obs}})}\\&=\frac{k^2(1+i)}{4\sqrt{k\pi}}\sum_{m=1}^{M}\mathcal{E}_m e^{ik\mathbf{d}\cdot\mathbf{r}_m}\sum_{n=1}^{N}e^{ik\boldsymbol{\theta}_n\cdot(\mathbf{r}_m-\mathbf{z})}\\&\approx\frac{k^2(1+i)}{4\sqrt{k\pi}}\sum_{m=1}^{M}\mathcal{E}_m e^{ik\mathbf{d}\cdot\mathbf{r}_m}\int_{\mathbb{S}^1_{\text{obs}}}e^{ik\boldsymbol{\theta}\cdot(\mathbf{r}_m-\mathbf{z})}d\boldsymbol{\theta}.\end{aligned} \tag{10}$$

The application of equations (6) and (10) yields that

$$\langle u_\infty(\boldsymbol{\theta},\mathbf{d}),e^{-ik\boldsymbol{\theta}\cdot\mathbf{z}}\rangle_{L^2(\mathbb{S}^1_{\text{obs}})}\approx\frac{k^2(1+i)(\theta_N-\theta_1)}{4\sqrt{k\pi}}\Big(\Phi_1(\mathbf{z},k)+\Lambda_1(\mathbf{z},k)\Big).$$

Finally, using Hölder's inequality,

$$\langle u_\infty(\boldsymbol{\theta},\mathbf{d}),e^{-ik\boldsymbol{\theta}\cdot\mathbf{z}}\rangle_{L^2(\mathbb{S}^1_{\text{obs}})}\le||u_\infty(\boldsymbol{\theta},\mathbf{d})||_{L^2(\mathbb{S}^1_{\text{obs}})}||e^{-ik\boldsymbol{\theta}\cdot\mathbf{z}}||_{L^2(\mathbb{S}^1_{\text{obs}})}, \tag{11}$$

we can obtain equation (7). This completes the proof. □

A. PROPERTIES OF AN INDICATOR FUNCTION

Based on the explored structure of indicator function, we can discover some properties of DSM and methods of improvement of DSM.

Observation 1: Based on the analyzed structure, i.e., equation (7), we observe that $J_0(k|\mathbf{r}_m-\mathbf{z}|)=1$ and $\Lambda_1(\mathbf{z},k)=0$ when $\mathbf{z}=\mathbf{r}_m\in\Sigma_m$. This is because $J_0(0)=1$ and $J_n(0)=0$, for $n=1,2,\cdots$. This means that it is possible to identify the location of Σ_m via the map of $\mathfrak{F}_{\text{DSM}}(\mathbf{z})$. Due to the oscillating property of the Bessel function, the terms $J_0(k|\mathbf{r}_m-\mathbf{z}|)$ and $\Lambda_1(\mathbf{z},k)$ are the main causative agents of generating some artifacts, and their appearance depend on the value of wavenumber, k.

Observation 2: It is noteworthy that the term $J_0(k|\mathbf{r}_m-\mathbf{z}|)$ is independent of the range of observation directions, but $\Lambda_1(\mathbf{z},k)$ significantly depends on the range of such directions. Thus, we can say that the terms $J_0(k|\mathbf{r}_m-\mathbf{z}|)$ and $\Lambda_1(\mathbf{z},k)$ contribute to and disturb the imaging performance, respectively. Hence, the key idea for improving the imaging accuracy is to eliminate or lower the magnitude of $\Lambda_1(\mathbf{z},k)$.

Observation 3: From (9), we can examine that

$$\Lambda_1(\mathbf{z},k)\propto\frac{1}{\theta_N-\theta_1}.$$

Thus, if the range of observation direction is wide, the effect of the term $\Lambda_1(\mathbf{z},k)$ becomes negligible; correspondingly, the imaging result will be good. Otherwise, if the range of such directions becomes narrow, the term $\Phi_1(\mathbf{z},k)$ becomes negligible and the term $\Lambda_1(\mathbf{z},k)$ can significantly affect the imaging performance.

Observation 4: Based on the structure of indicator function established in Theorem 1, it is possible to improve the imaging performance. The first way to improve it is by applying high frequency because, for sufficiently large k, the following asymptotic form holds:

$$J_s(k|\mathbf{r}-\mathbf{z}|)\approx\sqrt{\frac{2}{k\pi|\mathbf{r}-\mathbf{z}|}}\cos\left(k\pi|\mathbf{r}-\mathbf{z}|-\frac{s\pi}{2}-\frac{\pi}{4}\right). \tag{12}$$

We can observe that

$$\Lambda_1(\mathbf{z},k)=O\left(\frac{1}{(\theta_N-\theta_1)\sqrt{k|\mathbf{r}_m-\mathbf{z}|}}\right).$$

Hence, as $k\longrightarrow+\infty$, $\mathfrak{F}_{\text{DSM}}(\mathbf{z})=1$ at $\mathbf{z}=\mathbf{r}_m\in\Sigma_m$ and $\mathfrak{F}_{\text{DSM}}(\mathbf{z})=0$ at $\mathbf{z}\in\Omega\backslash\overline{\Sigma}$. Unfortunately, this is an ideal method.

Observation 5: Another way is to eliminate the disturbing term $\Lambda_1(\mathbf{z},k)$. Since $\mathbf{z}$ is arbitrary and $\mathbf{r}_m$ is unknown, we cannot control the value of $J_s(k|\mathbf{r}_m-\mathbf{z}|)$. Therefore, the condition on the range has to be set based on the following equation: for any integer s,

$$\cos\left(\frac{s\,(\theta_N+\theta_1-2\phi_m)}{2}\right)\sin\left(\frac{s(\theta_N-\theta_1)}{2}\right)=0. \tag{13}$$

One possible selection is $\theta_N-\theta_1=2\pi$, i.e., a full-aperture case. Based on [52], we have that

$$\mathfrak{F}_{\text{DSM}}(\mathbf{z})\approx\frac{|\Phi_1(\mathbf{z},k)|}{\max\limits_{\mathbf{z}\in\Omega}|\Phi_1(\mathbf{z},k)|}.$$

Therefore, one can obtain good imaging results since there is no disturbing term $\Lambda_1(\mathbf{z},k)$. Except for the full-aperture case, the other way to satisfy equation (13) is to set $\theta_N+\theta_1-2\phi_m=\pi$ and $\theta_N-\theta_1=\pi$. One possible solution is to choose $\theta_1=\phi_m$ and $\theta_N=\pi+\phi_m$ that satisfy equation (13). This means that one must to know *a priori* the information about Σ_m (i.e., value of ϕ_m), for all $m=1,2,\cdots,M$. Moreover, since ϕ_m depends both $\mathbf{z}$ and $\mathbf{r}_m$, selecting an optimal range of observation directions is difficult. Fortunately, if the range of the observation directions is wider than π, it will be possible to obtain a good result, as depicted in Figures 1 and 2.

IV. SIMULATION RESULTS: SINGLE-FREQUENCY CASE

Now, we validate the theoretical results by conducting various numerical simulations using both synthetic and experimental data. To compare the performances of the approaches, the Jaccard index [62], which measures the similarity of two finite sample sets A and B, is chosen. It is defined as follows:

$$J_{\text{IND}}(A,B)(\%)=\frac{|A\cap B|}{|A\cup B|}\times 100. \tag{14}$$

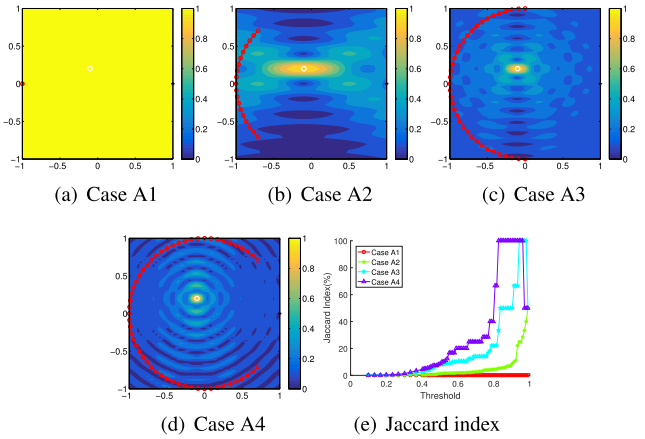

(a) Case A1 (b) Case A2 (c) Case A3

(d) Case A4 (e) Jaccard index

FIGURE 1. (Example 1) Maps of $\mathfrak{F}_{\mathrm{DSM}}(\mathbf{z})$ and Jaccard index with $f = 1$ GHz, where the red points represent θ_n.

Herein, the Jaccard index can be computed using $\mathfrak{F}^{\mathrm{EXACT}}(\mathbf{z})$ as a reference and the index map $\mathfrak{F}^{\kappa}(\mathbf{z})$ defined as a threshold, for $\kappa \in [0, 1]$, as follows:

$$\mathfrak{F}^{\mathrm{EXACT}}(\mathbf{z}) = \begin{cases} 1 & \text{for } \mathbf{z} \in \Sigma \\ 0 & \text{for } \mathbf{z} \in \mathbb{R}^2 \backslash \overline{\Sigma} \end{cases}$$

and

$$\mathfrak{F}^{\kappa}(\mathbf{z}) = \begin{cases} \mathfrak{F}_{\mathrm{DSM}}(\mathbf{z}) & \text{if } \mathfrak{F}_{\mathrm{DSM}}(\mathbf{z}) \geq \kappa \\ 0 & \text{if } \mathfrak{F}_{\mathrm{DSM}}(\mathbf{z}) < \kappa, \end{cases}$$

respectively. The Jaccard index $J_{\mathrm{IND}}(\mathfrak{F}^{\mathrm{EXACT}}, \mathfrak{F}^{\kappa})$ can be drawn as a function of the threshold level, κ.

A. SIMULATION RESULTS FROM SYNTHETIC DATA

A fixed frequency, $f = c/\lambda = 1$ GHz, is considered where $c = 1/\sqrt{\varepsilon_{\mathrm{b}}\mu_{\mathrm{b}}}$ denotes the speed of light and $\lambda \approx 0.3$ m. The far-field patterns are measured at N observation directions that are uniformly distributed on $\mathbb{S}^1_{\mathrm{obs}}$ for the single incident direction $\mathbf{d} = (-1, 0)$.

The range and the number of observation directions are defined by θ_1, θ_N, and N. The angle between two adjacent directions is given by $\Delta\theta = (\theta_N - \theta_1)/(N - 1)$. The various acquisition configurations are presented in Table 1.

The ROI, Ω, is a square of side length $20\lambda/3 = 2$ m uniformly discretized in 51×51 pixels. The far-field patterns $u_\infty(\boldsymbol{\theta}_n, \mathbf{d})$, for $n = 1, 2, \cdots, N$, are generated by FEldberechnung für Körper mit beliebiger Oberfläche (FEKO) and a 20 dB white Gaussian random noise is added using the MATLAB function awgn included in signal processing package.

Example 1 (Imaging of a Small Disk): First, we consider a single small dielectric disk with radius $\alpha \equiv 0.1\lambda = 0.03$ m and permittivity $\varepsilon \equiv 5\varepsilon_{\mathrm{b}}$. It is located at $\mathbf{r} = (-0.3333\lambda, 0.6667\lambda) = (-0.1\,\mathrm{m}, 0.2\,\mathrm{m})$

All the results obtained by combining the configurations presented in Table 1 are illustrated in Figure 2. Note that we cannot identify the inhomogeneities when there is only one receiver even if the number of sources is large and small.

TABLE 1. Values of θ_1, θ_N, and N used to obtained the synthetic data.

Cases	θ_1	θ_N	N	Description
Case A1	180°	180°	1	Single direction
Case A2	135°	225°	19	Narrow range
Case A3	90°	270°	37	Semi-circular range
Case A4	45°	315°	55	Wide but limited range

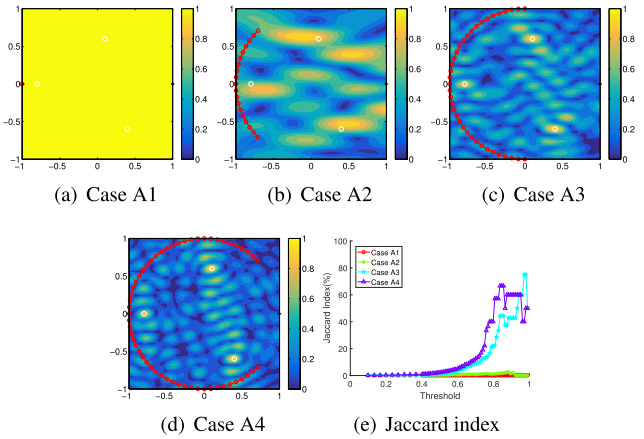

(a) Case A1 (b) Case A2 (c) Case A3

(d) Case A4 (e) Jaccard index

FIGURE 2. (Example 2) Maps of $\mathfrak{F}_{\mathrm{DSM}}(\mathbf{z})$ and Jaccard index with $f_0 = 1$ GHz, where the red points represent θ_n.

Additionally, all inhomogeneities cannot be identified if the observation range is too narrow as demonstrated in cases A1 and A2. In cases A3, A4, and A5 which satisfy $\pi \leq \theta_N - \theta_1 \leq 2\pi$, the inhomogeneities, Σ_m, can be identified via the map of $\mathfrak{F}_{\mathrm{DSM}}(\mathbf{z})$. Based on the Jaccard index (bottom row), it can be shown, as expected, that the larger the range of observation directions is, the better the results are.

Example 2 (Three Small Dielectric Disks With the Same Size and Permittivity): Here, we consider a group of three small dielectric disks Σ_m with $\alpha_m \equiv 0.1\lambda_0 = 0.03$ m and $\varepsilon_m \equiv 5\varepsilon_0$, $m = 1, 2, 3$. Their locations are $\mathbf{r}_1 = (-8\lambda_0/3, 0) = (-0.8\,\mathrm{m}, 0)$, $\mathbf{r}_2 = (4\lambda_0/3, -2\lambda_0) = (0.4\,\mathrm{m}, -0.6\,\mathrm{m})$, and $\mathbf{r}_3 = (\lambda_0/3, 2\lambda_0) = (0.1\,\mathrm{m}, 0.6\,\mathrm{m})$.

Figure 2 illustrates the results concerning the configurations presented in Table 1. Even though more oscillations are observed in the map of $\mathfrak{F}_{\mathrm{DSM}}(\mathbf{z})$ because of the interaction between inhomogeneities, the results are almost similar to those of Example 1.

Example 3 (Large Dielectric Disk): In this example, we investigate the feasibility of employing the DSM for imaging of a large target. Thus, we consider the imaging of a large disk located at $\mathbf{r} = (-\lambda_0, -\lambda_0)$ with radius $\alpha_m \equiv \lambda_0$. The dielectric permittivity is given by $\varepsilon \equiv 5\varepsilon_0$.

As shown in Figure 3, contrary to the results of Example 2, we cannot identify the exact shape and location from the map of $\mathfrak{F}_{\mathrm{DSM}}(\mathbf{z})$ with broad (i.e., $\theta_N - \theta_1 \geq \pi$) ranges of observation directions but with narrow range of incident directions. Hence, further improvement is required.

B. SIMULATION RESULTS FROM REAL DATA

In this subsection, we present some results from the Fresnel experimental data [53] to validate theoretical results.

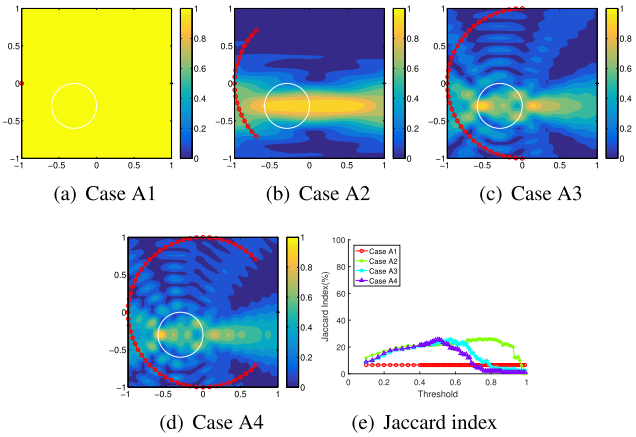

(a) Case A1 (b) Case A2 (c) Case A3

(d) Case A4 (e) Jaccard index

FIGURE 3. (Example 3) Maps of $\mathfrak{F}_{\mathrm{DSM}}(\mathbf{z})$ and Jaccard index with $f = 1$ GHz, where the red points represent θ_n.

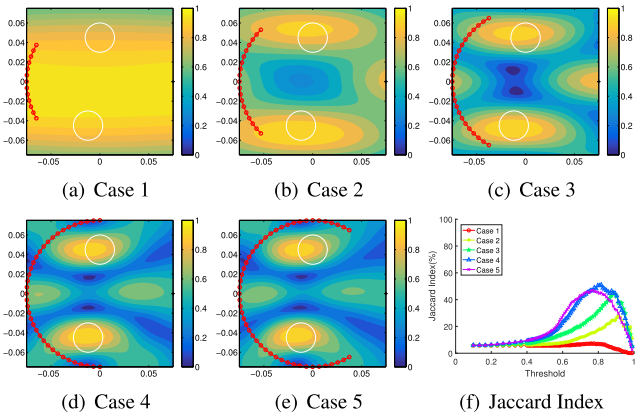

(a) Case 1 (b) Case 2 (c) Case 3

(d) Case 4 (e) Case 5 (f) Jaccard Index

FIGURE 4. (Example 4) Maps of $\mathfrak{F}_{\mathrm{DSM}}(\mathbf{z})$ and Jaccard index with $f = 4$ GHz, where the red points represent θ_n.

TABLE 2. Vales of θ_1 and θ_N, and N are utilized for the numerical simulations with experimental data.

Cases	θ_1	θ_N	N	Description
Case 1	150°	210°	12	Narrow range
Case 2	135°	225°	18	Narrow range
Case 3	120°	240°	24	Not narrow range
Case 4	90°	270°	36	Semi-circular range
Case 5	60°	300°	54	Wide but limited range

We consider the imaging of two dielectric cylinders at $f = 4$ GHz. The ROI, Ω, is set to a square of side length $4\lambda \approx 0.3$ m which is uniformly discretized with 51×51 pixels. We note the following:

- the full-aperture setting is not available due to the experimental configuration. In particular, the maximum range of observation directions is $\theta_1 = 60°$ and $\theta_N = 300°$ for $N = 49$.
- the scattered field was measured within the near-field configuration and cannot be approximated by the far-field pattern.

We refer to [53] for the additional details regarding the employed experimental set-up and various cases presented in Table 2.

Example 4 (Two Small Dielectric Disks With the Same Size and Permittivity): The locations of the targets are $(-0.012\,\mathrm{m}, -0.045\,\mathrm{m})$ and $(0\,\mathrm{m}, 0.045\,\mathrm{m})$. The radius and the dielectric permittivity are 0.015 m and $\varepsilon \propto 3\varepsilon_{\mathrm{b}}$, where ε_{b} denotes the background permittivity, respectively.

As depicted in Figure 4, the imaging performance of the DSM increases with respect to the range of the acquisition angle, verifying again our theoretical results and the related discussion in the Observation 3.

V. MDSM IN LIMITED-APERTURE PROBLEM

From the theory and simulation results above, we observe that it is possible to identify location Σ_m through the DSM but further improvements are still required because the imaging performance significantly depends on the range of observation directions. In numerous previously conducted studies [28], [49], [63], [64], the application of multiple frequencies yields results that are better than those obtained through the application of a single frequency. To obtain better results, we correspondingly consider the multi-frequency direct sampling method (MDSM). For this, we introduce an indicator function operated at numerous frequencies, f_p, $p = 1, 2, \cdots, P$, as follows:

$$\mathfrak{F}_{\mathrm{MDSM}}(\mathbf{z}) = \left| \frac{1}{P} \sum_{p=1}^{P} \frac{\langle u_\infty(\boldsymbol{\theta}_n, \mathbf{d}; k_p), e^{-ik_p \boldsymbol{\theta}_n \cdot \mathbf{z}} \rangle_{L^2(\mathbb{S}^1_{\mathrm{obs}})}}{||u_\infty(\boldsymbol{\theta}_n, \mathbf{d}; k_p)||_{L^2(\mathbb{S}^1_{\mathrm{obs}})} ||e^{-ik_p \boldsymbol{\theta}_n \cdot \mathbf{z}}||_{L^2(\mathbb{S}^1_{\mathrm{obs}})}} \right|, \quad (15)$$

where $u_\infty(\boldsymbol{\theta}, \mathbf{d}; k_p)$ denotes the far-field pattern defined in equation (1) at k_p, $p = 1, 2, \cdots, P$. Here, we set $k_1 < k_2 < \cdots < k_P$, and let $\mathbb{F}_p$ denote the set of measurement data

$$\mathbb{F}_p = \left\{ u_\infty(\boldsymbol{\theta}_n, \mathbf{d}; k_p) : p = 1, 2, \cdots, P, \ \boldsymbol{\theta}_n \in \mathbb{S}^1_{\mathrm{obs}} \right\}.$$

Notice that the improvement of multi-frequency based techniques has been validated on the basis of statistical hypothesis testing [28], [65], [66]. However, most of these are considered multi-static measurement configurations, so it is difficult to explain the improvement of $\mathfrak{F}_{\mathrm{MDSM}}(\mathbf{z})$. Instead, based on the fact that reducing the oscillating pattern of the Bessel function is a method of improvement, we explain why $\mathfrak{F}_{\mathrm{MDSM}}(\mathbf{z})$ is an improved version of $\mathfrak{F}_{\mathrm{DSM}}(\mathbf{z})$.

A. ANALYSIS OF IMAGING FUNCTION: SINGLE INHOMOGENEITY

For the sake of simplicity, let us consider the imaging of a single inhomogeneity $\Sigma = \mathbf{r} + \alpha\mathbf{D}$ with permittivity ε. We discuss the result in Theorem 2.

Theorem 2 (Single Inhomogeneity Case): Assume that the total number of applied frequencies, P, and observation directions, N, are large enough. Let $\mathbf{r} - \mathbf{z} = |\mathbf{r} - \mathbf{z}|(\cos\phi, \sin\phi)$. *Then,* $\mathfrak{F}_{\mathrm{MDSM}}(\mathbf{z})$ *can be represented as*

follows:

$$\mathfrak{F}_{\mathrm{MDSM}}(\mathbf{z}) \approx \frac{|\Phi_2(\mathbf{z}) + \Lambda_2(\mathbf{z})|}{\max\limits_{\mathbf{z}\in\Omega} |\Phi_2(\mathbf{z}) + \Lambda_2(\mathbf{z})|}, \tag{16}$$

where

$$\Phi_2(\mathbf{z}) = \frac{1}{k_P - k_1}\Big(\mathcal{S}(\mathbf{z}, k_P) - \mathcal{S}(\mathbf{z}, k_1)\Big)$$

and

$$\Lambda_2(\mathbf{z}) = \sum_{p=1}^{P} \Lambda_1'(\mathbf{z}, k_p) \approx \int_{k_1}^{k_P} \Lambda_1'(\mathbf{z}, k)dk.$$

Here,

$$\begin{aligned}&\mathcal{S}(\mathbf{z}, k)\\ &= kJ_0(k|\mathbf{r}-\mathbf{z}|) + \frac{k\pi}{2}\\ &\quad\times\Big(J_1(k|\mathbf{r}-\mathbf{z}|)S_0(k|\mathbf{r}-\mathbf{z}|) - J_0(k|\mathbf{r}-\mathbf{z}|)S_1(k|\mathbf{r}-\mathbf{z}|)\Big)\end{aligned}$$

and

$$\begin{aligned}\Lambda_1'(\mathbf{z}, k) = \frac{4}{\theta_N - \theta_1}\sum_{s=1}^{\infty}\frac{i^s}{s}J_s(k|\mathbf{r}_m - \mathbf{z}|)\\ \times\cos\frac{s\,(\theta_N + \theta_1 - 2\phi_m)}{2}\sin\frac{s(\theta_N - \theta_1)}{2},\end{aligned}$$

where S_n denotes the Struve function of integer order n and for sufficiently large $\mathcal{N}_1 \in \mathbb{N}$,

$$\Lambda_2(\mathbf{z}) = O\left(\frac{1}{\mathcal{N}_1(\theta_N - \theta_1)}\right). \tag{17}$$

Proof: Based on Theorem 1, we have

$$\begin{aligned}&\langle u_\infty(\boldsymbol{\theta}_n, \mathbf{d}, k_p), e^{-ik_p\boldsymbol{\theta}_n\cdot\mathbf{z}}\rangle_{L^2(\mathbb{S}^1_{\mathrm{obs}})}\\ &\qquad\approx \frac{k_p^2(1+i)(\theta_N - \theta_1)}{4\sqrt{k_p\pi}}\Big(\Phi_1(\mathbf{z}, k_p) + \Lambda_1(\mathbf{z}, k_p)\Big),\end{aligned}$$

where $\Phi_1(\mathbf{z}, k_p)$ and $\Lambda_1(\mathbf{z}, k_p)$ are defined in (8) and (9), respectively. With this, we observe that

$$\begin{aligned}\frac{1}{P}\sum_{p=1}^{P}\frac{\langle u_\infty(\boldsymbol{\theta}_n, \mathbf{d}, k_p), e^{-ik_p\boldsymbol{\theta}_n\cdot\mathbf{z}}\rangle_{L^2(\mathbb{S}^1_{\mathrm{obs}})}}{||u_\infty(\boldsymbol{\theta}_n, \mathbf{d}, k_p)||_{L^2(\mathbb{S}^1_{\mathrm{obs}})}||e^{-ik_p\boldsymbol{\theta}_n\cdot\mathbf{z}}||_{L^2(\mathbb{S}^1_{\mathrm{obs}})}}\\ = \frac{1}{P}\sum_{p=1}^{P}\Big(J_0(k_p|\mathbf{r}-\mathbf{z}|) + \Lambda_1'(\mathbf{z}, k_p)\Big).\end{aligned}$$

Since P and N are sufficiently large, the following indefinite integral of the Bessel function holds (see [67]):

$$\int J_0(x)dx = xJ_0(x) + \frac{x\pi}{2}\Big(J_1(x)H_0(x) - J_0(x)H_1(x)\Big).$$

We can immediately observe that

$$\begin{aligned}\frac{1}{P}\sum_{p=1}^{P}J_0(k_p|\mathbf{r}-\mathbf{z}|) &= \frac{1}{k_P - k_1}\int_{k_1}^{k_P}J_0(k|\mathbf{r}-\mathbf{z}|)dk\\ &= \frac{1}{k_P - k_1}\Big(\mathcal{S}(\mathbf{z}, k_P) - \mathcal{S}(\mathbf{z}, k_1)\Big).\end{aligned}$$

Based on the uniform convergence of Jacobi-Anger expansion, $\Lambda_1(\mathbf{z}, k)$ converges uniformly. Thus, for every positive real number ϵ, there exists a sufficiently large natural number, $\mathcal{N}_1 \in \mathbb{N}$, such that

$$\begin{aligned}&\left|\Lambda_1'(\mathbf{z}, k_p) - \frac{4}{\theta_N - \theta_1}\sum_{s=1}^{\mathcal{N}_1}\frac{i^s}{s}J_s(k_p|\mathbf{r}-\mathbf{z}|)\right.\\ &\left.\quad\times\sin\left(\frac{s(\theta_N - \theta_1)}{2}\right)\cos\left(\frac{s(\theta_N + \theta_1 - 2\phi)}{2}\right)\right| < \epsilon.\end{aligned} \tag{18}$$

This means that

$$\begin{aligned}&\frac{1}{P}\sum_{p=1}^{P}\Lambda_1'(\mathbf{z}, k_p)\\ &\approx \int_{k_1}^{k_P}\Lambda_1'(\mathbf{z}, k)dk\\ &= \frac{4}{(\theta_N - \theta_1)(k_P - k_1)}\sum_{s=1}^{\mathcal{N}_1}\frac{i^s}{s}\sin\left(\frac{s(\theta_N - \theta_1)}{2}\right)\\ &\quad\times\cos\left(\frac{s(\theta_N + \theta_1 - 2\phi)}{2}\right)\int_{k_1}^{k_P}J_s(k|\mathbf{r}-\mathbf{z}|)dk.\end{aligned}$$

Now, assume that $\mathbf{z}$ approaches to $\mathbf{r}$, then $J_s(k|\mathbf{r}-\mathbf{z}|) \longrightarrow 0$, for all $s = 1, 2, \cdots, \mathcal{N}_1$. Consequently, $\sum_{p=1}^{P}\Lambda_1'(\mathbf{z}, k_p)$ becomes negligible. Assume that $\mathbf{z}$ is located away from $\mathbf{r}$ such that $k_1|\mathbf{r}-\mathbf{z}| \gg \mathcal{N}_1^2 - 0.25$. Then, based on (12),

$$\int_{k_1}^{k_P}|J_s(k|\mathbf{r}-\mathbf{z}|)|dk \ll \frac{\sqrt{2}(k_P - k_1)}{\sqrt{(\mathcal{N}_1^2 - 0.25)\pi}},$$

we obtain that

$$\begin{aligned}\left|\sum_{p=1}^{P}\Lambda_1'(\mathbf{z}, k_p)\right| &\ll \frac{4\sqrt{2}\mathcal{N}_1}{(\theta_N - \theta_1)\sqrt{(\mathcal{N}_1^2 - 0.25)\pi}}\\ &\le \frac{4\sqrt{2}}{\mathcal{N}_1(\theta_N - \theta_1)\sqrt{\pi}} = O\left(\frac{1}{\mathcal{N}_1(\theta_N - \theta_1)}\right).\end{aligned}$$

Hence, we can obtain (16) and (17). □

B. PROPERTIES OF INDICATOR FUNCTION

Now, we discuss some properties of the $\mathfrak{F}_{\mathrm{MDSM}}(\mathbf{z})$, and compare its imaging performance with the $\mathfrak{F}_{\mathrm{DSM}}(\mathbf{z})$.

Observation 6: Since $(\mathcal{S}(\mathbf{z}, k_P) - \mathcal{S}(\mathbf{z}, k_1))/(k_P - k_1) = 1$ (see Figure 5) and $\Lambda_1(\mathbf{z}, k_p) = 0$, for $p = 1, 2, \cdots, P$, when $\mathbf{z} = \mathbf{r} \in \Sigma$, then map of $\mathfrak{F}_{\mathrm{MDSM}}(\mathbf{z})$ contains maximum amplitude at $\mathbf{z} = \mathbf{r} \in \Sigma$. However, some artifacts still exist in the map of $\mathfrak{F}_{\mathrm{MDSM}}(\mathbf{z})$. Note that the appearance of unexpected artifacts highly depends on the range of observation directions and total number of applied frequencies. For the detail, if the range of observation directions is narrow or the total number of applied frequencies, P, is small, then the artifacts that show up can disturb the recognition of the location of inhomogeneities, while good imaging results can be retrieved if the range is wide and the total number is large enough.

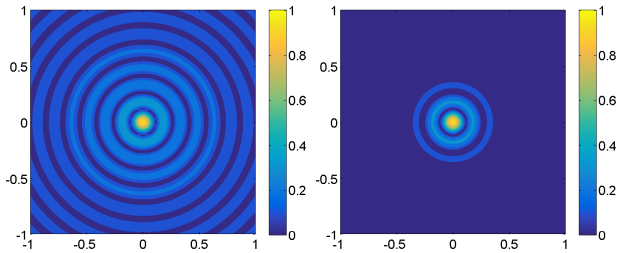

(a) $|J_0(k|\mathbf{z}|)|$ (b) $\left|\frac{\mathcal{S}(\mathbf{z},k_P)-\mathcal{S}(\mathbf{z},k_1)}{k_P-k_1}\right|$

FIGURE 5. Two-dimensional plots of $|J_0(k|\mathbf{z}|)|$ for $f = 1$ GHz and $|(\mathcal{S}(\mathbf{z}, k_P) - \mathcal{S}(\mathbf{z}, k_1))/(k_P - k_1)|$ for $f_1 = 700$ MHz and $f_P = 1.3$ GHz.

Observation 7: Similar to the properties of a single-frequency DSM discussed in the Observation 2, the contributing term of MDSM, $(\mathcal{S}(\mathbf{z}, k_P) - \mathcal{S}(\mathbf{z}, k_1))/(k_P - k_1)$, is also independent of the range of observation directions, whereas the disturbing term $\int_{k_1}^{k_P} \Lambda_1(\mathbf{z}, k)dk$ is not. This implies that we have to reduce the effect of $\int_{k_1}^{k_P} \Lambda_1(\mathbf{z}, k)dk$ to improve the imaging performance.

Observation 8: In the full-aperture configuration ($\theta_N - \theta_1 = 2\pi$), we can observe that

$$\mathfrak{F}_{\mathrm{DSM}}(\mathbf{z}) \propto |J_0(k|\mathbf{r} - \mathbf{z}|)|$$

and

$$\mathfrak{F}_{\mathrm{MDSM}}(\mathbf{z}) \propto |\mathcal{S}(\mathbf{z}, k_P) - \mathcal{S}(\mathbf{z}, k_1)|\,.$$

This implies that MDSM exhibits a better imaging performance than the single-frequency DSM due to oscillation patterns, as demonstrated in Figure 5. A similar phenomenon can be examined in the case of limited-aperture problem.

C. SIMULATION RESULTS

To validate the result of Theorem 2 and several properties discussed above, we conduct several numerical simulations. For multiple frequencies, we consider 7 frequencies ranging from $f_1 = 700\,\mathrm{MHz}$ to $f_P = 1.3\,\mathrm{GHz}$ with step size $\triangle f = 100\,\mathrm{MHz}$ and 8 frequencies ranging from 1 GHz to 8 GHz with a step size of 1 GHz for synthetic and experimental data, respectively.

The accuracies of the methods are compared using Jaccard index (14) where $\mathfrak{F}(\mathbf{z})$ represents $\mathfrak{F}_{\mathrm{MDSM}}(\mathbf{z})$. For the configuration, we recall Table 1 for Examples 5, 6, and 7 with synthetic data.

Example 5 (Small Dielectric Disk): Here, we consider the imaging of a small dielectric disk, Σ, with radius $\alpha \equiv 0.1\lambda_0 = 0.03\,\mathrm{m}$ and permittivity $\varepsilon \equiv 5\varepsilon_0$. It is located at $\mathbf{r} = (-0.3333\lambda_0, 0.6667\lambda_0) = (-0.1\,\mathrm{m}, 0.2\,\mathrm{m})$.

By applying $\mathfrak{F}_{\mathrm{MDSM}}(\mathbf{z})$, we obtain the imaging result depicted in figure 6. This result shows that the location of inhomogeneity, Σ, is successfully identified by employing the map of $\mathfrak{F}_{\mathrm{MDSM}}(\mathbf{z})$. Furthermore, the results of the Jaccard index demonstrate that it is an improved version

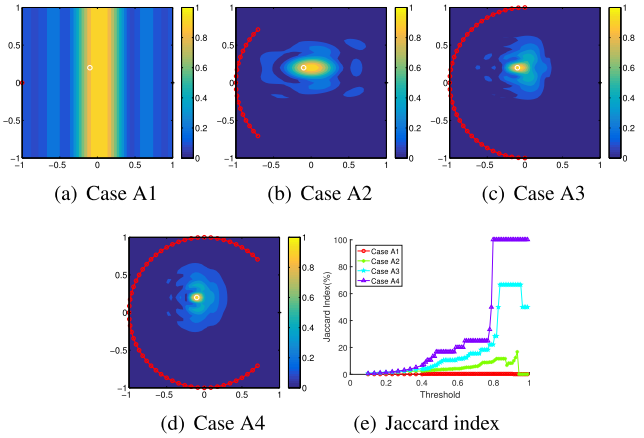

(a) Case A1 (b) Case A2 (c) Case A3

(d) Case A4 (e) Jaccard index

FIGURE 6. (Example 5) Maps of $\mathfrak{F}_{\mathrm{MDSM}}(\mathbf{z})$ and Jaccard index with $f = \{700\,\mathrm{MHz}, 800\,\mathrm{GHz}, \cdots, 1.3\,\mathrm{GHz}\}$, where the red points represent θ_n.

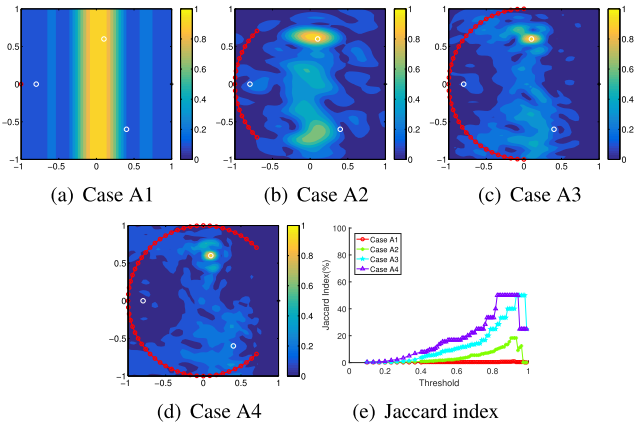

(a) Case A1 (b) Case A2 (c) Case A3

(d) Case A4 (e) Jaccard index

FIGURE 7. (Example 6) Maps of $\mathfrak{F}_{\mathrm{MDSM}}(\mathbf{z})$ and Jaccard index with $f = \{700\,\mathrm{MHz}, 800\,\mathrm{GHz}, \cdots, 1.3\,\mathrm{GHz}\}$, where the red points represent θ_n.

of DSM (compare to Figure 1) as stated in the Observation 8. However, the result of $\mathfrak{F}_{\mathrm{MDSM}}(\mathbf{z})$ is not significantly improved since the total number and range of incident fields are increased. On the other hand, when more numerous and various incident fields are considered, the imaging performance of $\mathfrak{F}_{\mathrm{MDSM}}(\mathbf{z})$ can be improved.

Example 6 (Three Small Dielectric Disks With the Same Size and Permittivity): Based on the information of inhomogeneities from Example 2, Σ_m with $\alpha_m \equiv 0.1\lambda_0 = 0.03\,\mathrm{m}$ and $\varepsilon_m \equiv 5\varepsilon_0$, $m = 1, 2, 3$. The locations, $\mathbf{r}_m$, of Σ_m are as follows: $\mathbf{r}_1 = (-8\lambda_0/3, 0) = (-0.8\,\mathrm{m}, 0)$, $\mathbf{r}_2 = (4\lambda_0/3, -2\lambda_0) = (0.4\,\mathrm{m}, -0.6\,\mathrm{m})$, and $\mathbf{r}_2 = (\lambda_0/3, 2\lambda_0) = (0.1\,\mathrm{m}, 0.6\,\mathrm{m})$.

Based on Figure 7, we observe that $\mathfrak{F}_{\mathrm{MDSM}}(\mathbf{z})$ cannot be applied for imaging of multiple inhomogeneities even with a wide range of incident directions. Sometimes, although the multi-frequency based technique is known as an improved version, it is impossible to identify the location of inhomogeneities via $\mathfrak{F}_{\mathrm{MDSM}}(\mathbf{z})$. We can also examine similar result in microwave imaging, refer to [50].

Example 7 (Large Dielectric Disk): The location and size of a large inhomogeneity are $\mathbf{r} = (-\lambda_0, -\lambda_0) =$

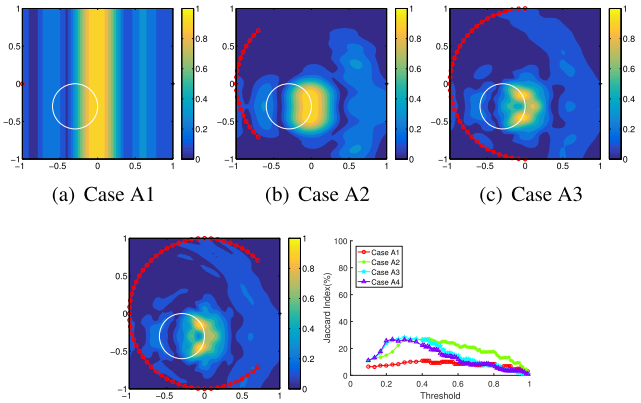

(a) Case A1 (b) Case A2 (c) Case A3

(d) Case A4 (e) Jaccard index

FIGURE 8. (Example 7) Maps of $\mathfrak{F}_{\mathrm{MDSM}}(\mathbf{z})$ and Jaccard index, where the red points represent θ_n.

$(-0.3\,\mathrm{m}, -0.3\,\mathrm{m})$ and $\alpha_m \equiv \lambda_0 = 0.3\,\mathrm{m}$, respectively. The dielectric permittivity is given by $\varepsilon \equiv 5\varepsilon_0$.

As we already seen, a single small target can be visualized in the map of $\mathfrak{F}_{\mathrm{MDSM}}(\mathbf{z})$, whereas a large target cannot even visualized with a wide range of incident directions (Figure 8). This result shows the fundamental limitation of MDSM and explains that an improvement is still needed.

D. ANALYSIS OF IMAGING FUNCTION: MULTIPLE INHOMOGENEITIES

Based on the Example 6, some inhomogeneities cannot be recognized via MDSM. This means that some phenomena still cannot be explained by the Theorem 2. Thus, further analysis of imaging function in the presence of multiple inhomogeneities is required to explain the phenomena where the location cannot be found. The theoretical reason is the following.

Theorem 3 (Multiple Inhomogeneities Case): Assume that there exists several inhomogeneities Σ_m and the total numbers of receivers, N, and frequencies, P, are sufficiently large. Let $\mathbf{d}\cdot\mathbf{r}_m = |\mathbf{r}_m|\cos\psi_m$ and $\mathbf{r}_m - \mathbf{z} = |\mathbf{r}_m - \mathbf{z}|(\cos\phi_m, \sin\phi_m)$. Then, $\mathfrak{F}_{\mathrm{MDSM}}(\mathbf{z})$ can be represented as follows:

$$\mathfrak{F}_{\mathrm{MDSM}}(\mathbf{z}) \approx \frac{|\Phi_3(\mathbf{z})|}{\max\limits_{\mathbf{z}\in\Omega}|\Phi_3(\mathbf{z})|},$$

where

$$\Phi_3(\mathbf{z}) = \sum_{m=1}^{M} \frac{\alpha_m^2(\varepsilon_m - \varepsilon_0)}{(k_P - k_1)\sqrt{\varepsilon_b\mu_b}}\left(\Phi_3^{(1)}(\mathbf{z}) + \Phi_3^{(2)}(\mathbf{z}) + \Phi_3^{(3)}(\mathbf{z})\right)$$

with

$$\Phi_3^{(2)}(\mathbf{z}) = 2\sum_{t=1}^{\infty}\cos(t\psi_m)\int_{k_1}^{k_P} J_0(k|\mathbf{r}_m - \mathbf{z}|)J_t(k|\mathbf{r}_m|)dk,$$

$$\Phi_3^{(3)}(\mathbf{z}) = \frac{1}{k_P - k_1}\int_{k_1}^{k_P}\Lambda_1(\mathbf{z}, k) \times \left(J_0(k|\mathbf{r}_m|) + 2\sum_{t=1}^{\infty}\cos(t\psi_m)J_t(k|\mathbf{r}_m|)\right)dk,$$

and

1) *if* $|\mathbf{r}_m| = |\mathbf{r}_m - \mathbf{z}|$ *then*

$$\Phi_3^{(1)}(\mathbf{z}) = k_P\left(J_0(k_P|\mathbf{r}_m - \mathbf{z}|)^2 + J_1(k_P|\mathbf{r}_m - \mathbf{z}|)^2\right) - k_1\left(J_0(k_1|\mathbf{r}_m - \mathbf{z}|)^2 + J_1(k_1|\mathbf{r}_m - \mathbf{z}|)^2\right) + \int_{k_1}^{k_P} J_0(k|\mathbf{r}_m - \mathbf{z}|)dk, \tag{19}$$

2) *if* $|\mathbf{r}_m| > |\mathbf{r}_m - \mathbf{z}|$ *then*

$$\Phi_3^{(1)}(\mathbf{z}) = \Psi_2(|\mathbf{r}_m|, |\mathbf{r}_m - \mathbf{z}|, k_P) - \Psi_2(|\mathbf{r}_m|, |\mathbf{r}_m - \mathbf{z}|, k_1), \tag{20}$$

3) *if* $|\mathbf{r}_m| < |\mathbf{r}_m - \mathbf{z}|$ *then*

$$\Phi_3^{(1)}(\mathbf{z}) = \Psi_2(|\mathbf{r}_m - \mathbf{z}|, |\mathbf{r}_m|, k_P) - \Psi_2(|\mathbf{r}_m - \mathbf{z}|, |\mathbf{r}_m|, k_1). \tag{21}$$

Here,

$$\Psi_2(\alpha, \beta, k) = \sum_{s=1}^{\infty}\frac{(-1)^s(\alpha^2 - \beta^2)}{(s!)^2 4^s(2s+1)}L_s\left(\frac{\alpha^2 + \beta^2}{\alpha^2 - \beta^2}\right)k^{2s+1}$$

and L_s denotes a Legendre polynomial of order s. Furthermore, if $0 < k_P|\mathbf{r}_m - \mathbf{z}| \ll \sqrt{2}$, then

$$\frac{1}{k_P - k_1}\int_{k_1}^{k_P} J_1(k|\mathbf{r}_m - \mathbf{z}|)^2 dk \ll O(1).$$

Additionally, for sufficiently large $\mathcal{N} \in \mathbb{N}$,

$$|\Phi_3^{(2)}(\mathbf{z})| = O\left(\frac{1}{\mathcal{N}(\theta_N - \theta_1)}\right).$$

Proof: Based on the result in Theorem 1, we can observe that

$$\sum_{p=1}^{P}\frac{\langle u_\infty(\boldsymbol{\theta}_n, \mathbf{d}, k_p), e^{-ik_p\boldsymbol{\theta}_n\cdot\mathbf{z}}\rangle_{L^2(\mathbb{S}^1_{\mathrm{obs}})}}{||u_\infty(\boldsymbol{\theta}_n, \mathbf{d}, k_p)||_{L^2(\mathbb{S}^1_{\mathrm{obs}})}||e^{-ik_p\boldsymbol{\theta}_n\cdot\mathbf{z}}||_{L^2(\mathbb{S}^1_{\mathrm{obs}})}} \approx \frac{|\Phi_3(\mathbf{z})|}{\max\limits_{\mathbf{z}\in\Omega}|\Phi_3(\mathbf{z})|},$$

where

$$\Phi_3(\mathbf{z}) = \sum_{m=1}^{M}\frac{\alpha_m^2(\varepsilon_m - \varepsilon_0)}{(k_P - k_1)\sqrt{\varepsilon_b\mu_b}}\left(\Phi_3^{(1)}(\mathbf{z}) + \Phi_3^{(2)}(\mathbf{z}) + \Phi_3^{(3)}(\mathbf{z})\right)$$

with

$$\Phi_3^{(1)}(\mathbf{z}) = \frac{1}{P}\sum_{p=1}^{P} J_0(k_p|\mathbf{r}_m|)J_0(k_p|\mathbf{r}_m - \mathbf{z}|),$$

$$\Phi_3^{(2)}(\mathbf{z}) = 2\sum_{t=1}^{\infty}\cos(t\psi_m)\left[\frac{1}{P}\sum_{p=1}^{P} J_0(k_p|\mathbf{r}_m - \mathbf{z}|)J_t(k_p|\mathbf{r}_m|)\right],$$

$$\Phi_3^{(3)}(\mathbf{z}) = \frac{1}{P}\sum_{p=1}^{P}\Lambda_1(\mathbf{z}, k_p) \times \left(J_0(k_p|\mathbf{r}_m|) + 2\sum_{t=1}^{\infty}\cos(t\psi_m)J_t(k_p|\mathbf{r}_m|)\right).$$

Since P is sufficiently large, then the following relations hold (see [67]):

$$\int J_0(x)^2 dx = x\Big(J_0(x)^2 + J_1(x)^2\Big) + \int J_1(x)^2 dx$$

and

$$\int_0^x J_0(\alpha t)J_0(\beta t)dt = \sum_{s=1}^{\infty} \frac{(-1)^s(\alpha^2-\beta^2)}{(s!)^2 4^s(2s+1)} \times L_s\left(\frac{\alpha^2+\beta^2}{\alpha^2-\beta^2}\right) x^{2s+1}, \quad \beta < \alpha.$$

Consequently, we can obtain (19), (20), and (21). Analogously, since P is sufficiently large, it follows that

$$\Phi_3^{(2)}(\mathbf{z}) = \frac{2}{k_P - k_1} \sum_{t=1}^{\infty} \cos(t\psi_m) \int_{k_1}^{k_P} J_0(k|\mathbf{r}_m - \mathbf{z}|) J_t(k|\mathbf{r}_m|) dk$$

and

$$\Phi_3^{(3)}(\mathbf{z}) = \frac{1}{k_P - k_1} \int_{k_1}^{k_P} \Lambda_1(\mathbf{z}, k) \times \left(J_0(k|\mathbf{r}_m|) + 2\sum_{t=1}^{\infty} \cos(t\psi_m) J_t(k|\mathbf{r}_m|) \right) dk.$$

Assume that $0 < k_P|\mathbf{r}_m - \mathbf{z}| \ll \sqrt{2}$. Then, the following asymptotic form holds, for small arguments $0 < x \ll \sqrt{s+1}$:

$$J_s(x) \approx \frac{1}{\Gamma(s+1)} \left(\frac{x}{2}\right)^s, \tag{22}$$

where $\Gamma(x)$ denotes the Gamma function. Therefore, we have that

$$\int_{k_1}^{k_P} J_1(k|\mathbf{r}_m - \mathbf{z}|)^2 dk \ll O(k_P)$$

and, correspondingly

$$\frac{1}{k_P - k_1} \int_{k_1}^{k_P} J_1(k|\mathbf{r}_m - \mathbf{z}|)^2 dk \ll O(1).$$

Now, by utilizing inequality (18), then there exists a large number, $\mathcal{N}_\star \in \mathbb{N}$, such that

$$\frac{1}{k_P - k_1} \int_{k_1}^{k_P} J_0(k|\mathbf{r}_m|)\Lambda_1(\mathbf{z}, k) dk = \frac{4}{(k_P - k_1)(\theta_N - \theta_1)} \sum_{s=1}^{\mathcal{N}_\star} \frac{i^s}{s} \cos\left(\frac{s(\theta_N + \theta_1 - 2\phi_m)}{2}\right) \times \sin\left(\frac{s(\theta_N - \theta_1)}{2}\right) \int_{k_1}^{k_P} J_0(k|\mathbf{r}_m|) J_s(k|\mathbf{r}_m - \mathbf{z}|) dk.$$

Assume that $\mathbf{z}$ is sufficiently close to $\mathbf{r}_m$, such that $k_P|\mathbf{z} - \mathbf{r}_m| \ll \sqrt{\mathcal{N}_\star + 1}$. Then, by using (22), we get that

$$\int_{k_1}^{k_P} J_0(k|\mathbf{r}_m|) J_s(k|\mathbf{r}_m - \mathbf{z}|) dk \le \frac{|\mathbf{r}_m - \mathbf{z}|^s}{2^s s!} \int_{k_1}^{k_P} |k|^s dk \le \frac{(k_P^{s+1} - k_1^{s+1})|\mathbf{r}_m - \mathbf{z}|^s}{2^s(s+1)!} \ll \frac{k_P\sqrt{\mathcal{N}_\star + 1}}{2^s(s+1)!}.$$

According to [68, p. 362, 9.1.62], for $x \in \mathbb{R}$, we have the following inequality:

$$J_s(x) \le \frac{|x|^s}{2^s s!}, \quad x \in \mathbb{R}.$$

By applying Hölder's inequality, we obtain that

$$\int_{k_1}^{k_P} J_0(k|\mathbf{r}_m|) J_s(k|\mathbf{r}_m - \mathbf{z}|) dk \le \frac{|\mathbf{r}_m - \mathbf{z}|^s}{2^s s!} \int_{k_1}^{k_P} |k|^s dk \le \frac{(k_P^{s+1} - k_1^{s+1})|\mathbf{r}_m - \mathbf{z}|^s}{2^s(s+1)!}.$$

If $\mathbf{z}$ is far away from $\mathbf{r}_m$ such that $k_1|\mathbf{z} - \mathbf{r}_m| \gg \mathcal{N}_\star^2 - 0.25$, then the application of (12) yields

$$\begin{aligned}
&\int_{k_1}^{k_P} J_0(k|\mathbf{r}_m|) J_s(k|\mathbf{r}_m - \mathbf{z}|) dk \\
&\le \int_{k_1}^{k_P} \sqrt{\frac{2}{k\pi|\mathbf{r}_m - \mathbf{z}|}} \cos\left(k|\mathbf{r}_m - \mathbf{z}| - \frac{s\pi}{2} - \frac{\pi}{4}\right) dk \\
&\le \sqrt{\frac{2}{\pi|\mathbf{r}_m - \mathbf{z}|}} (\sqrt{k_P} - \sqrt{k_1}) \le k_P \sqrt{\frac{2}{k_P \pi |\mathbf{r}_m - \mathbf{z}|}} \\
&\le k_P \sqrt{\frac{2}{\pi|\mathcal{N}_\star^2 - 0.25|}}.
\end{aligned}$$

Based on the uniform convergence of Jacobi-Anger expansion, there exist large numbers, $\mathcal{N}_1, \mathcal{N}_2 \in \mathbb{N}$, such that

$$\frac{1}{P} \sum_{p=1}^{P} \Lambda_1(\mathbf{z}, k_p) J_0(k_p|\mathbf{r}_m|) \le O\left(\frac{1}{\mathcal{N}_1(\theta_N - \theta_1)}\right)$$

and

$$\frac{2}{P} \sum_{p=1}^{P} \Lambda_1(\mathbf{z}, k_p) \left(\sum_{t=1}^{\infty} \cos(t\psi_m) J_t(k_p|\mathbf{r}_m|) \right) \le O\left(\frac{1}{\mathcal{N}_2(\theta_N - \theta_1)}\right).$$

Hence, by setting $\mathcal{N} = \min\{\mathcal{N}_1, \mathcal{N}_2\}$ and applying Hölder's inequality (11), we obtain that

$$|\Phi_3^{(2)}(\mathbf{z})| = O\left(\frac{1}{\mathcal{N}(\theta_N - \theta_1)}\right).$$

This completes the proof. □

Now, based on our structure analysis verified in Theorem 3, we elucidate the reason of the unexpected phenomena demonstrated in Figure 7 as follows.

Remark 1 (Limitation of $\mathfrak{F}_{\mathrm{MDSM}}(\mathbf{z})$ for Imaging of Multiple Inhomogeneities): Contrary to the result of $\mathfrak{F}_{\mathrm{MDSM}}(\mathbf{z})$ for imaging a single inhomogeneity, $\mathfrak{F}_{\mathrm{MDSM}}(\mathbf{z})$ comprises the following three terms: $\Phi_3^{(1)}(\mathbf{z})$, $\Phi_3^{(2)}(\mathbf{z})$, and $\Phi_3^{(3)}(\mathbf{z})$. Note that $\Phi_3^{(3)}(\mathbf{z}) = 0$ if $\mathbf{z} = \mathbf{r}_m$.

Now, we focus on the behavior of $\Phi_3^{(1)}(\mathbf{z})$ and $\Phi_3^{(2)}(\mathbf{z})$ when $\mathbf{z} = \mathbf{r}_m \neq \mathbf{0}$. Since $\mathbf{r}_m$ is fixed and $|\mathbf{r}_m| > 0$, it follows that

$$\begin{aligned}\Phi_3^{(1)}(\mathbf{z}) &= \sum_{s=1}^{\infty} \frac{(-1)^s}{(s!)^2 4^s (2s+1)} |\mathbf{r}_m|^{2s} L_s(1)(k_P^{2s+1} - k_1^{2s+1}) \\ &= {}_1\mathrm{F}_2\left(\frac{1}{2}; 1, \frac{3}{2}; \frac{|\mathbf{r}_m|^2 k_P^2}{4}\right) k_P \\ &\quad - {}_1\mathrm{F}_2\left(\frac{1}{2}; 1, \frac{3}{2}; \frac{|\mathbf{r}_m|^2 k_1^2}{4}\right) k_1, \end{aligned} \tag{23}$$

where ${}_a\mathrm{F}_b$ denotes the generalized hypergeometric function of orders a and b. Furthermore, based on the integral of Bessel function (see [69]), $\Phi_3^{(2)}(\mathbf{z})$ can be written as follows:

$$\begin{aligned}\Phi_3^{(2)}(\mathbf{z}) &= 2\sum_{t=1}^{\infty} \cos(t\psi_m) \int_{k_1}^{k_P} J_t(k|\mathbf{r}_m|)dk \\ &= \sum_{t=1}^{\infty} \frac{\cos(t\psi_m)}{2^{t-1}\Gamma(t+2)} \\ &\quad \times \left\{ {}_1\mathrm{F}_2\left(\frac{t+1}{2}; t+1, \frac{t+3}{2}; -\frac{1}{4}k_P^2|\mathbf{r}_m|^2\right) k_P \right. \\ &\quad \left. - {}_1\mathrm{F}_2\left(\frac{t+1}{2}; t+1, \frac{t+3}{2}; -\frac{1}{4}k_1^2|\mathbf{r}_m|^2\right) k_1 \right\}, \end{aligned} \tag{24}$$

Hence, by employing equations (23) and (24), and properties of the hypergeometric functions, there exist m and m' such that for $m \neq m'$,

$$\mathfrak{F}_{\mathrm{MDSM}}(\mathbf{r}_m; \mathbf{d}) \neq \mathfrak{F}_{\mathrm{MDSM}}(\mathbf{r}_{m'}; \mathbf{d}).$$

Therefore, the map of $\mathfrak{F}_{\mathrm{MDSM}}(\mathbf{z})$ has different amplitudes at each of the locations of the inhomogeneities even if their physical properties (e.g., permittivity, size, shape, etc) are the same. This is the theoretical reason why sometimes we cannot identify all the inhomogeneities by applying the map of $\mathfrak{F}_{\mathrm{MDSM}}(\mathbf{z})$.

Based on remark 1, we can conclude that one must apply numerous incident fields to overcome this limitation. We refer to [28], [52], [70], [71] for related works.

VI. CONCLUSION

This study considered the DSM with a single-incident field in a limited-aperture inverse scattering problem. By utilizing the asymptotic formula of far-field pattern, the mathematical structure of the indicator functions for single- and MDSM in the limited-aperture problem was identified. We explored the fact that DSM is related to the infinite series of Bessel function of integer orders, range of observation and incident directions, and physical information about targets (e.g., location, shape, size, and electrical permittivity). To improve imaging performance, the indicator function of MDSM was introduced and analyzed when only a single small homogeneity exists in the medium and theoretically proved that it can be represented by an infinite series of Bessel functions of integer order and Struve function. However, the indicator function cannot be applied in the case of numerous well-separated inhomogeneities. To elucidate this theory, the mathematical structure of indicator function of MDSM for multiple inhomogeneities was analyzed by establishing a relationship with an infinite series of the Bessel functions of integer order, Legendre polynomial, and generalized hypergeometric function. Various numerical simulations with synthetic and experimental data were conducted to support our theoretical results.

Throughout theoretical and simulation results, we cannot say that the imaging results via DSM and MDSM with single incident field do not guarantee complete shaping of the inhomogeneities. However, we believe that they could be a good initial guess of a standard iterative techniques as mentioned in the introduction.

In this study, we considered the imaging of small and large targets. In the future, we hope to study an application for the imaging of arbitrarily shaped targets. Furthermore, real-world applications still have some limitations. We believe that the application of numerous incident fields can guarantee better results. In future work, we hope to improve the DSM to obtain better results.

ACKNOWLEDGMENT

The authors would like to acknowledge Dominique Lesselier for his valuable comments. The constructive comments of anonymous reviewers are acknowledged.

REFERENCES

[1] E. J. Baranoski, "Through-wall imaging: Historical perspective and future directions," *J. Franklin Inst.*, vol. 345, no. 6, pp. 556–569, Sep. 2008.
[2] D. Kim, B. Kim, and S. Nam, "A dual-band through-the-wall imaging radar receiver using a reconfigurable high-pass filter," *J. Electromagn. Eng. Sci.*, vol. 16, no. 3, pp. 164–168, Jul. 2016.
[3] F. Soldovieri and R. Solimene, "Through-wall imaging via a linear inverse scattering algorithm," *IEEE Geosci. Remote Sens. Lett.*, vol. 4, no. 4, pp. 513–517, Oct. 2007.
[4] M.-A. Ploix, V. Garnier, D. Breysse, and J. Moysan, "NDE data fusion to improve the evaluation of concrete structures," *NDT E Int.*, vol. 44, no. 5, pp. 442–448, Sep. 2011.
[5] C. Völker and P. Shokouhi, "Multi sensor data fusion approach for automatic honeycomb detection in concrete," *NDT E Int.*, vol. 71, pp. 54–60, Apr. 2015.
[6] S. K. Verma, S. S. Bhadauria, and S. Akhtar, "Review of nondestructive testing methods for condition monitoring of concrete structures," *J. Const. Eng*, vol. 2013, Mar. 2013, Art. no. 834572.
[7] T. Rubaek, P. M. Meaney, P. Meincke, and K. D. Paulsen, "Nonlinear microwave imaging for breast-cancer screening using Gauss-Newton's method and the CGLS inversion algorithm," *IEEE Trans. Antennas Propag.*, vol. 55, no. 8, pp. 2320–2331, Aug. 2007.
[8] N. Irishina, M. Moscoso, and O. Dorn, "Microwave imaging for early breast cancer detection using a shape-based strategy," *IEEE Trans. Biomed. Eng.*, vol. 56, no. 4, pp. 1143–1153, Apr. 2009.
[9] M. Haynes, J. Stang, and M. Moghaddam, "Microwave breast imaging system prototype with integrated numerical characterization," *Int. J. Biomed. Imag.*, vol. 2012, pp. 1–18, Jan. 2012.
[10] A. S. Fokas, Y. Kurylev, and V. Marinakis, "The unique determination of neuronal currents in the brain via magnetoencephalography," *Inverse Problems*, vol. 20, no. 4, pp. 1067–1082, Aug. 2004.
[11] T. Seo, S. Oh, D. Jung, Y. Huh, J. Cho, and Y. Kwon, "Noninvasive brain stimulation using a modulated microwave signal," *J. Electromagn. Eng. Sci.*, vol. 18, no. 1, pp. 70–72, Jan. 2018.
[12] M. Salucci, J. Vrba, I. Merunka, and A. Massa, "Real-time brain stroke detection through a learning-by-examples technique—An experimental assessment," *Microw. Opt. Technol. Lett.*, vol. 59, no. 11, pp. 2796–2799, Nov. 2017.

[13] I. Catapano, F. Soldovieri, and L. Crocco, "2D GPR imaging via linear sampling method: A performance assessment tool," in *Proc. 6th Int. Workshop Adv. Ground Penetrating Radar (IWAGPR)*, Jun. 2011, pp. 1–4.
[14] X. Liu, M. Serhir, and M. Lambert, "Detectability of junctions of underground electrical cables with a ground penetrating radar: Electromagnetic simulation and experimental measurements," *Construct. Building Mater.*, vol. 158, pp. 1099–1110, Jan. 2018.
[15] P. A. Torrione, K. D. Morton, R. Sakaguchi, and L. M. Collins, "Histograms of oriented gradients for landmine detection in ground-penetrating radar data," *IEEE Trans. Geosci. Remote Sens.*, vol. 52, no. 3, pp. 1539–1550, Mar. 2014.
[16] L. Zhang, M. Xing, C.-W. Qiu, J. Li, J. Sheng, Y. Li, and Z. Bao, "Resolution enhancement for inversed synthetic aperture radar imaging under low SNR via improved compressive sensing," *IEEE Trans. Geosci. Remote Sens.*, vol. 48, no. 10, pp. 3824–3838, Oct. 2010.
[17] M. Cetin, I. Stojanovic, O. Onhon, K. Varshney, S. Samadi, W. C. Karl, and A. S. Willsky, "Sparsity-driven synthetic aperture radar imaging: Reconstruction, autofocusing, moving targets, and compressed sensing," *IEEE Signal Process. Mag.*, vol. 31, no. 4, pp. 27–40, Jul. 2014.
[18] T. Zhang and X.-G. Xia, "OFDM synthetic aperture radar imaging with sufficient cyclic prefix," *IEEE Trans. Geosci. Remote Sens.*, vol. 53, no. 1, pp. 394–404, Jan. 2015.
[19] F. Tilmann, "Seismic imaging of the downwelling indian lithosphere beneath central tibet," *Science*, vol. 300, no. 5624, pp. 1424–1427, May 2003.
[20] Y. Chen, J. Yuan, S. Zu, S. Qu, and S. Gan, "Seismic imaging of simultaneous-source data using constrained least-squares reverse time migration," *J. Appl. Geophys.*, vol. 114, pp. 32–35, Mar. 2015.
[21] Z. Xue, Y. Chen, S. Fomel, and J. Sun, "Seismic imaging of incomplete data and simultaneous-source data using least-squares reverse time migration with shaping regularization," *Geophysics*, vol. 81, no. 1, pp. S11–S20, Jan. 2016.
[22] R. Chandra, H. Zhou, I. Balasingham, and R. M. Narayanan, "On the opportunities and challenges in microwave medical sensing and imaging," *IEEE Trans. Biomed. Eng.*, vol. 62, no. 7, pp. 1667–1682, Jul. 2015.
[23] O. Dorn and D. Lesselier, "Level set methods for inverse scattering," *Inverse Problems*, vol. 22, no. 4, pp. R67–R131, Aug. 2006.
[24] R. Kress, "Inverse scattering from an open arc," *Math. Methods Appl. Sci.*, vol. 18, no. 4, pp. 267–293, Apr. 1995.
[25] C. Y. Ahn, K. Jeon, and W.-K. Park, "Analysis of MUSIC-type imaging functional for single, thin electromagnetic inhomogeneity in limited-view inverse scattering problem," *J. Comput. Phys.*, vol. 291, pp. 198–217, Jun. 2015.
[26] H. Ammari, E. Iakovleva, and D. Lesselier, "A MUSIC algorithm for locating small inclusions buried in a half-space from the scattering amplitude at a fixed frequency," *Multiscale Model. Simul.*, vol. 3, no. 3, pp. 597–628, Jan. 2005.
[27] Y.-D. Joh, Y. M. Kwon, and W.-K. Park, "MUSIC-type imaging of perfectly conducting cracks in limited-view inverse scattering problems," *Appl. Math. Comput.*, vol. 240, pp. 273–280, Aug. 2014.
[28] H. Ammari, J. Garnier, H. Kang, W.-K. Park, and K. Sølna, "Imaging schemes for perfectly conducting cracks," *SIAM J. Appl. Math.*, vol. 71, no. 1, pp. 68–91, Jan. 2011.
[29] W.-K. Park, "Multi-frequency subspace migration for imaging of perfectly conducting, arc-like cracks in full- and limited-view inverse scattering problems," *J. Comput. Phys.*, vol. 283, pp. 52–80, Feb. 2015.
[30] W.-K. Park, "Real-time microwave imaging of unknown anomalies via scattering matrix," *Mech. Syst. Signal Process.*, vol. 118, pp. 658–674, Mar. 2019.
[31] C. Y. Ahn, K. Jeon, Y.-K. Ma, and W.-K. Park, "A study on the topological derivative-based imaging of thin electromagnetic inhomogeneities in limited-aperture problems," *Inverse Problems*, vol. 30, no. 10, Oct. 2014, Art. no. 105004.
[32] M. Bonnet, "Fast identification of cracks using higher-order topological sensitivity for 2-D potential problems," *Eng. Anal. Boundary Elements*, vol. 35, no. 2, pp. 223–235, Feb. 2011.
[33] F. Le Louër and M.-L. Rapún, "Topological sensitivity for solving inverse multiple scattering problems in three-dimensional Electromagnetism. Part I: One step method," *SIAM J. Imag. Sci.*, vol. 10, no. 3, pp. 1291–1321, Jan. 2017.
[34] H. Ammari, M. Asch, L. G. Bustos, V. Jugnon, and H. Kang, "Transient wave imaging with limited-view data," *SIAM J. Imag. Sci.*, vol. 4, no. 4, pp. 1097–1121, Jan. 2011.
[35] B. T. Cox, S. R. Arridge, and P. C. Beard, "Photoacoustic tomography with a limited-aperture planar sensor and a reverberant cavity," *Inverse Problems*, vol. 23, no. 6, pp. S95–S112, Dec. 2007.
[36] M. Ikehata, E. Niemi, and S. Siltanen, "Inverse obstacle scattering with limited-aperture data," *Inverse Problems Imag.*, vol. 6, no. 1, pp. 77–94, 2012.
[37] Y. M. Kwon and W.-K. Park, "Analysis of subspace migrations in limited-view inverse scattering problems," *Appl. Math. Lett.*, vol. 26, no. 12, pp. 1107–1113, 2013.
[38] R. Mager and N. Bleistein, "An examination of the limited aperture problem of physical optics inverse scattering," *IEEE Trans. Antennas Propag.*, vol. 26, pp. 695–699, Sep. 1978.
[39] R. L. Ochs, Jr., "The limited aperture problem of inverse acoustic scattering: Dirichlet boundary conditions," *SIAM J. Appl. Math.*, vol. 47, no. 6, pp. 1320–1341, Dec. 1987.
[40] A. Zinn, "On an optimisation method for the full- and the limited-aperture problem in inverse acoustic scattering for a sound-soft obstacle," *Inverse Problems*, vol. 5, no. 2, pp. 239–253, Apr. 1989.
[41] E. Miller, M. Cheney, M. Kilmer, G. Boverman, A. Li, and D. Boas, "Feature-enhancing inverse methods for limited-view tomographic imaging problems," *Subsurface Sens. Technol. Appl.*, vol. 4, no. 4, pp. 327–353, 2003.
[42] W.-K. Park, "Detection of small electromagnetic inhomogeneities with inaccurate frequency," *J. Korean Phys. Soc.*, vol. 68, no. 5, pp. 607–615, Mar. 2016.
[43] W.-K. Park and D. Lesselier, "Electromagnetic MUSIC-type imaging of perfectly conducting, arc-like cracks at single frequency," *J. Comput. Phys.*, vol. 228, no. 21, pp. 8093–8111, Nov. 2009.
[44] W.-K. Park and D. Lesselier, "MUSIC-type imaging of a thin penetrable inclusion from its multi-static response matrix," *Inverse Problems*, vol. 25, no. 7, Jul. 2009, Art. no. 075002.
[45] K. Ito, B. Jin, and J. Zou, "A direct sampling method to an inverse medium scattering problem," *Inverse Problems*, vol. 28, no. 2, Feb. 2012, Art. no. 025003.
[46] J. Li and Z. Zou, "A direct sampling method for inverse scattering using far-field data," *Inverse Problems Imag.*, vol. 7, no. 3, pp. 757–775, 2013.
[47] W.-K. Park, "Direct sampling method for anomaly imaging from scattering parameter," *Appl. Math. Lett.*, vol. 81, pp. 63–71, Jul. 2018.
[48] S. Kang, M. Lambert, and W.-K. Park, "Analysis and improvement of direct sampling method in the monostatic configuration," *IEEE Geosci. Remote Sens. Lett.*, vol. 16, no. 11, pp. 1721–1725, Nov. 2019.
[49] W.-K. Park, "Improvement of direct sampling method in transverse electric polarization," *Appl. Math. Lett.*, vol. 88, pp. 209–215, Feb. 2019.
[50] W.-K. Park, "Negative result of multi-frequency direct sampling method in microwave imaging," *Results Phys.*, vol. 12, pp. 859–860, Mar. 2019.
[51] S.-H. Son, K.-J. Lee, and W.-K. Park, "Application and analysis of direct sampling method in real-world microwave imaging," *Appl. Math. Lett.*, vol. 96, pp. 47–53, Oct. 2019.
[52] S. Kang, M. Lambert, and W.-K. Park, "Direct sampling method for imaging small dielectric inhomogeneities: Analysis and improvement," *Inverse Problems*, vol. 34, no. 9, Sep. 2018, Art. no. 095005.
[53] K. Belkebir and M. Saillard, "Special section: Testing inversion algorithms against experimental data," *Inverse Problems*, vol. 17, no. 6, pp. 1565–1571, Dec. 2001.
[54] R. Potthast, "A study on orthogonality sampling," *Inverse Problems*, vol. 26, no. 7, Jul. 2010, Art. no. 074015.
[55] R. Griesmaier, "Multi-frequency orthogonality sampling for inverse obstacle scattering problems," *Inverse Problems*, vol. 27, no. 8, Aug. 2011, Art. no. 085005.
[56] M. T. Bevacqua, T. Isernia, R. Palmeri, M. N. Akinci, and L. Crocco, "Physical insight unveils new imaging capabilities of orthogonality sampling method," *IEEE Trans. Antennas Propag.*, vol. 68, no. 5, pp. 4014–4021, May 2020.
[57] C. Y. Ahn, S. Chae, and W.-K. Park, "Fast identification of short, sound-soft open arcs by the orthogonality sampling method in the limited-aperture inverse scattering problem," *Appl. Math. Lett.*, vol. 109, Nov. 2020, Art. no. 106556.
[58] I. Harris and D.-L. Nguyen, "Orthogonality sampling method for the electromagnetic inverse scattering problem," *SIAM J. Sci. Comput.*, vol. 42, no. 3, pp. B722–B737, Jan. 2020.

[59] D. L. Colton and R. Kress, *Inverse Acoustic and Electromagnetic Scattering Theory*, 2nd ed. Cham, Switzerland: Springer, 1998.
[60] H. Ammari and H. Kang, *Reconstruction of Small Inhomogeneities from Boundary Measurements* (Lecture Notes in Mathematics), vol. 1846. Berlin, Germany: Springer-Verlag, 2004.
[61] M. Slaney, A. C. Kak, and L. E. Larsen, "Limitations of imaging with first-order diffraction tomography," *IEEE Trans. Microw. Theory Techn.*, vol. 32, no. 8, pp. 860–874, Aug. 1984.
[62] P. Jaccard, "The distribution of the flora in the alpine Zone.1," *New Phytologist*, vol. 11, no. 2, pp. 37–50, Feb. 1912.
[63] B. B. Guzina, F. Cakoni, and C. Bellis, "On the multi-frequency obstacle reconstruction via the linear sampling method," *Inverse Problems*, vol. 26, no. 12, Dec. 2010, Art. no. 125005.
[64] R. Griesmaier and C. Schmiedecke, "A multifrequency MUSIC algorithm for locating small inhomogeneities in inverse scattering," *Inverse Problems*, vol. 33, no. 3, Mar. 2017, Art. no. 035015.
[65] H. Ammari, J. Garnier, W. Jing, H. Kang, M. Lim, K. Solna, and H. Wang, *Mathematical and Statistical Methods for Multistatic Imaging*. Cham, Switzerland: Springer, 2010.
[66] H. Ammari, *Mathematical Modeling in Biomedical Imaging II Optical, Ultrasound, and Opto-Acoustic Tomographies* (Lecture Notes in Mathematics), vol. 2035. Berlin, Germany: Springer, 2011.
[67] W. Rosenheinrich. (2019). *Tables of Some Indefinite Integrals of Bessel Functions*. [Online]. Available: http://www.fh-jena.de/~rsh/Forschung/Stoer/besint.pdf
[68] M. Abramowitz and I. Stegun, *Handbook of Mathematical Functions With Formulas, Graphs, and Mathematical Tables* (Applied Mathematics Series 55). Washington, DC, USA: Nat. Bur. Standards, 1964.
[69] Y. L. Luke, *Integrals of Bessel Functions*. Chelmsford, MA, USA: Courier Corporation, 2014.
[70] X. Liu, "A novel sampling method for multiple multiscale targets from scattering amplitudes at a fixed frequency," *Inverse Problems*, vol. 33, no. 8, Aug. 2017, Art. no. 085011.
[71] W.-K. Park, "Direct sampling method for retrieving small perfectly conducting cracks," *J. Comput. Phys.*, vol. 373, pp. 648–661, Nov. 2018.

SANGWOO KANG received the M.S. degree in mathematics from Yonsei University, Seoul, South Korea, in 2015, and the Ph.D. degree in electrical engineering from University of Paris-Sud, University of Paris-Saclay, France, in 2019. He is currently a Postdoctoral Researcher at the COMELEC Department, Télécom Paris, France. His research interests include applied mathematics, inverse problem, microwave imaging, and scientific computing.

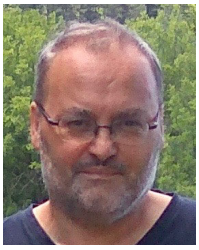

MARC LAMBERT received the Ph.D. degree in optics and photonics and the H.D.R. degree from the University of Paris-Sud, Orsay, France, in 1994 and 2001, respectively. From 1995 to 2014, he carried out his research activities within the L2S, CNRS, Paris, France, as a Charge de Recherche, and he has been with the Group of Electrical Engineering, Paris, since 2015. His research interests include the solutions of direct and inverse scattering problems in electromagnetics and acoustics, and their applications to the characterization of objects buried in complex environments from limited datasets.

CHI YOUNG AHN received the B.S., M.S., and Ph.D. degrees in mathematics from Yonsei University, Seoul, South Korea, in 1999, 2001, and 2011, respectively. He is currently a Senior Researcher and serves as the Director of the Medical Mathematics Division, National Institute for Mathematical Sciences. His research interests include industrial mathematics, medical imaging, and image processing.

TAEYOUNG HA received the M.S. and Ph.D. degrees in mathematics from Seoul National University, Seoul, South Korea. He was a Researcher with the Geophysics Laboratory, Seoul National University, Seoul, in 2000. He is currently a Principal Researcher at the Division of Medical Mathematics, National Institute for Mathematical Sciences. His research interests include numerical analysis, scientific computing, inverse problems, and data analysis.

WON-KWANG PARK received the M.S. degree in mathematics from Yonsei University, Seoul, South Korea, in 2004, and the Ph.D. degree in applied mathematics from the École Polytechnique, Palaiseau, France, in 2009. After graduation, he joined the Institute for Mathematics and Scientific Computing, Karl Franzens University of Graz, Austria, as a Postdoctoral Researcher, in 2009. In 2010, he joined the Department of Mathematics, Kookmin University, as a full-time Lecturer, where he is currently a Full Professor at the Department of Information Security, Cryptology, and Mathematics. His research interests include microwave imaging, electromagnetics, and scientific computing and related inverse problems.